

Contents lists available at ScienceDirect

# Journal of Energy Chemistry

JOURNAL OF ENERGY CHEMISTRY

http://www.journals.elsevier.com/ iournal-of-energy-chemistry

journal homepage: www.elsevier.com/locate/jechem

# Effects of silver-doping on properties of Cu(In,Ga)Se<sub>2</sub> films prepared by CuInGa precursors

Chen Wang <sup>a</sup>, Daming Zhuang <sup>a,b,c,\*</sup>, Ming Zhao <sup>a,b,c,\*</sup>, Yuxian Li <sup>a</sup>, Liangzheng Dong <sup>a</sup>, Hanpeng Wang <sup>a</sup>, Jinquan Wei <sup>a,b,c</sup>, Qianming Gong <sup>a,b,c</sup>

- <sup>a</sup> School of Materials Science and Engineering, Tsinghua University, Beijing 100084, China
- b Key Lab. for Advanced Materials Processing Technology of Ministry of Education, Tsinghua University, Beijing 100084, China
- <sup>c</sup>State Key Lab. of New Ceramics and Fine Processing, Tsinghua University, Beijing 100084, China

# ARTICLE INFO

#### Article history: Received 3 May 2021 Revised 26 July 2021 Accepted 5 August 2021 Available online 13 August 2021

Keywords: CIGS solar cell Ag doping Selenization Sputtering Cu-Ag-In-Ga precursor Defects

#### ABSTRACT

The AgCuInGa alloy precursors with different Ag concentrations are fabricated by sputtering an Ag target and a CuInGa target. The precursors are selenized in the  $H_2$ Se-containing atmosphere to prepare (Ag,Cu) (In,Ga)Se $_2$  (ACIGS) absorbers. The beneficial effects of Ag doping are demonstrated and their mechanism is explained. It is found that Ag doping significantly improves the films crystallinity. This is believed to be due to the lower melting point of chalcopyrite phase obtained by the Ag doping. This leads to a higher migration ability of the atoms that in turn promotes grain boundary migration and improves the film crystallinity. The Ga enrichment at the interface between the absorber and the back electrode is also alleviated during the selenization annealing. It is found that Ag doping within a specific range can passivate the band tail and improve the quality of the films. Therefore, carrier recombination is reduced and carrier transport is improved. The negative effects of excessive Ag are also demonstrated and their origin is revealed. Because the atomic size of Ag is different from that of Cu, for the Ag/(Ag + Cu) ratio (AAC)  $\geq 0.030$ , lattice distortion is aggravated, and significant micro-strain appears. The atomic radius of Ag is close to those of In and Ga, so that the continued increase in AAC will give rise to the Ag<sub>In</sub> or Ag<sub>Ga</sub> defects. Both the structural and compositional defects degrade the quality of the absorbers and the device performance. An excellent absorber can be obtained at AAC of 0.015.

© 2021 Science Press and Dalian Institute of Chemical Physics, Chinese Academy of Sciences. Published by ELSEVIER B.V. and Science Press. All rights reserved.

#### 1. Introduction

 $\text{Cu(In,Ga)Se}_2$  (CIGS-based) solar cell has been a key member in the family of thin film solar cells. In recent years, great progress has been achieved in the field of CIGS cells for both small-area laboratory cells and modules, resulting in ongoing performance improvement and increasing commercialization of these devices [1–5].

The concentration of Cu in the CIGS absorber strongly affects the quality of the absorber and the device performance and must be controlled to be in the appropriate range. Specifically, it should be slightly lower than the stoichiometric ratio in order to obtain the desired conduction type because CIGS films require Cu vacancies ( $V_{\text{Cu}}$ ) to form a p-type semiconductor [6]. However,  $In_{\text{Cu}}$  or  $Ga_{\text{Cu}}$  substitution defects may appear if the Cu concentration is

E-mail addresses: dmzhuang@tsinghua.edu.cn (D. Zhuang), zhaoming2013@-mail.tsinghua.edu.cn (M. Zhao).

too low. These defects then can form defect pairs with  $V_{\text{Cu}}$  and give rise to carrier loss [7,8]. On the other hand, a Cu-rich absorber is favorable for improving the crystallinity of the CIGS absorber, resulting in the reduction of boundary defects [9]. However, excessive Cu will not only reduce the concentration of  $V_{\text{Cu}}$ , but also leads to the formation of the Cu-Se secondary phase in the film [10]. The phase acts as a carrier recombination center and may even change the conduction type of the films if the Cu concentration is too high [10,11]. Therefore, Cu concentration is a key parameter and should be controlled in a narrow range in order to obtain a high-quality absorber. If the concentration deviates from this range, the film performance will deteriorate rapidly. In the actual film fabrication process, the grains are generally still not sufficiently large when the negative effects caused by excessive Cu begin to appear [10–12].

In the very early studies on the fabrication of CIGS absorbers by the co-evaporation method, KCN has been usually used to etch the film with a specific Cu distribution [13]. This method can simultaneously remove the Cu-Se phase and obtain large grains. Compared

<sup>\*</sup> Corresponding authors.

to the co-evaporation method, sputtering is a more straightforward and less expensive production process and can achieve better composition uniformity for large-area films [14]. However, in contrast to the co-evaporation method, it is difficult to control the Cu distribution of the films fabricated by sputtering. Due to its high toxicity, the use of KCN is restricted so that KCN etching cannot be used to control the Cu distribution in industrial production of CIGS films. Therefore, to enable low-cost industrial production of CIGS films using the sputtering method, it is necessary to increase the grain size of the films.

It is well-known that elements belonging to the same group have the same number of valence electrons, and therefore often have similar chemical properties. Both Cu and Ag belong to the IB group, so that AgInSe and CuInSe are both semiconductor materials that can be used as photovoltaic absorber films [1,15]. However, since Ag and Cu belong to different periods, the properties of the AgInSe and CuInSe compounds differ in some aspects.

Ag-doped CIGS has attracted intense attention of several research groups [16–20]. According to the reports in the literature, the partial substitution of Cu by Ag can improve the performances of the absorbers. The use of different amounts of Ag doping in different studies reported in the literature has led to large variations in the film properties. Such large variation may be caused by the different methods used for film fabrication.

Many studies on the Ag-doped CIGS fabricated by the coevaporation [16,17], solution methods [19] and by annealing CIGS precursors deposited by the sputtering of CIGS ceramic targets [20] have been reported. Comparison of the solution method and the annealing of ceramic precursors shows that selenization annealing of the CuInGa precursors can obtain films with relatively larger grains [21]. Therefore, this method may require less Ag, reducing the cost of the films. However, to date, there have been few reports on the Ag-doped CIGS absorbers fabricated by selenization annealing of the Ag-doped CuInGa precursors deposited by the sputtering alloy targets.

In addition, most reports in the literature [16,19] discuss the beneficial effects of Ag by comparing the samples with and without added Ag. Many reports only consider the changes due to Ag doping but ignore the difference between the effects of Ag and Cu. In fact, increasing the Cu concentration within an appropriate range can also improve the quality of the film. Therefore, a comparative study of the effects of the two elements is necessary to further explore effects of Ag doping and obtain more accurate conclusions.

Most reported films in literature also suffer from the adverse effects of excessive Ag doping and the appropriate Ag doping range has not been specified. To determine the appropriate Ag doping range, it is necessary to conduct a more thorough study and analysis of the effects of the Ag doping amount.

In this work, precursors with different Ag concentrations were fabricated by sputtering CuInGa and Ag targets followed by annealing in the  $H_2Se/Ar$  atmosphere. The film quality and device performances were characterized. For some films, Cu was used to replace the added Ag to further explore the effects of Ag on film quality.

### 2. Experimental

#### 2.1. Preparation of absorbers and devices

Molybdenum films (thickness of approximately 800 nm) were deposited on soda-lime glass (SLG) by DC-sputtering, followed by the deposition of precursor films. The precursor films were fabricated in two steps. In the first step, Ag or Cu was sputtered onto the Mo-coated SLG substrate layer. Then in the second step, CulnGa films (thickness of approximately 600 nm) were deposited by sputtering a CulnGa alloy target. Thus, the films with different compo-

sitions can be obtained by controlling the amount of Ag or Cu in the first step. As a whole, the value of Ga/(In + Ga) in films is about 0.30. In this work, I/III is used to represent the ratio of the concentration of group I element to the concentration of group III element in both the precursors and absorbers. AAC is the abbreviation of Ag/(Ag + Cu). Table 1 shows the fabricated samples and their corresponding samples ID, I/III, and AAC. A in sample ID indicates that the samples were fabricated by growing the Ag film in the first step, while C indicates that the samples were fabricated by growing the Cu film in the step.

The precursor films were annealed in a selenization furnace. The furnace chamber was evacuated to a base vacuum of  $2.0\times10^{-3}$  Pa prior to selenization. Then,  $H_2Se$  as the Se source and balance Ar as the carrier gas were introduced into the furnace to form the selenization atmosphere during the annealing process. The  $H_2Se$  concentration was 5.0 vol%. The samples were first heated to the temperature of 300 °C at a rate of 20 °C/min and were kept for 40 min at this temperature to carry out preliminary selenization that is a key process for homogeneous selenization. Then, the temperature was raised to 540 °C for the final selenization for 40 min. Then, the samples were cooled by furnace cooling after the completion of the final selenization.

The deposition of other layers and the fabrication of solar cell devices are the same as in our previous works [22]. CdS (thickness of approximately 50 nm) films were fabricated by chemical bath deposition (CBD), followed by i-ZnO (80 nm)/AZO (350 nm) window layers that were manufactured by sputtering the targets at 200°C. No metal grid and anti-reflective coating were used in this work. The devices were divided into separate cells by mechanical scribing with an effective area of 0.25 cm<sup>2</sup>.

#### 2.2. Characterization

Field emission scanning electronic microscopy (FE-SEM, Zeiss Sigma, Germany) equipped with EDS accessory was used to investigate the morphologies of the samples. A differential scanning calorimeter (DSC, Netzsch STA 449F3, Germany) was used to determine the melting temperature. The phases were determined by Raman spectroscopy (Horiba LabRAM HR Evolution) with a 532 nm wavelength laser and by X-ray diffraction (XRD, Rigaku Smartlab, Japan) using Cu  $K\alpha$  radiation ( $\lambda$  = 1.5418 Å) in  $\theta$ -2 $\theta$  mode. The photoluminescence (PL) spectra were recorded using a spectrophotometer excited by a 900 nm laser at room temperature. Urbach energy  $(E_{II})$  was estimated from the external quantum efficiency (EQE) data that were measured using the QTest Station 2000ADI system (Crowntech Inc., USA). The system was calibrated by the standard Si and the In-Ga-As photodiodes. Electrochemical impedance spectroscopy (EIS) measurements were carried out using an electrochemical workstation (Zahner IM6) at the frequencies from 10 Hz to 8 MHz. The current density-voltage (J-V) curves were measured with a solar simulator (Class AAA, Newport) under AM 1.5G illumination (1000 W/m<sup>2</sup>) after calibration with a refer-

**Table 1**The I/III and AAC of the fabricated samples.

Sample ID	I/III	AAC
A0	0.843	0
A1	0.849	0.008
A2	0.856	0.015
A4	0.869	0.030
A6	0.881	0.044
C6	0.881	0
A20	0.971	0.132
C20	0.971	0

ence Si solar cell under the same conditions. All of the experiments were performed at room temperature.

#### 3. Results and discussion

Large grains are beneficial for the performances of CIGS thin film solar cells [23–25]. Small grains lead to a greater amount of grain boundaries that give rise to the scattering of the carriers during charge carrier transport. In addition, the structure and phase composition at the grain boundaries are relatively complex, and the presence of many grain boundaries will increase the carrier recombination rate. Fig. 1 shows the SEM images of the ACIGS films with different Ag concentrations that were used to evaluate the influence of Ag addition on grain growth. The results show that the grain sizes increase monotonically with the AAC increasing from 0 to 0.044. The growth of the grains is the result of the grain boundary migration. Since grain boundary migration strongly depends on the diffusion of atoms, the diffusion ability of atoms has a significant impact on grain growth.

It has been reported that Cu can combine with Se to form the Cu-Se phase [10,13]. During the annealing process, Cu-Se will exist as the liquid phase due to its low melting point. The liquid phase can promote the diffusion of atoms, thereby promoting the growth of crystal grains. This also shows that Cu promotes increased grain size. To explore the effects of Ag doping on grain growth and compare the difference between Ag and Cu in promoting grain growth, the Ag added in the sample A6 was replaced by the same amount of Cu. Comparison of Fig. 1(a and f) shows that the Cu-added film has larger grains than the film without added Cu, but its crystallinity is not better than that of the A6 film.

To further explore the difference between Cu and Ag in promoting grain growth, CuSe, CuInSe<sub>2</sub>, Ag<sub>2</sub>Se and AgInSe<sub>2</sub> were examined by DSC. The results of the DSC measurements are shown in Fig. 2.

Fig. 2(a-1) shows the DSC curve of CuSe. Two endothermic peaks are observed, with the endothermic peak at low temperature corresponding to the decomposition of CuSe to Cu<sub>2</sub>Se and Se and the broader peak at a higher temperature corresponding to the melting peak of the remaining CuSe. The melting point of CuSe reported in related literature is approximately 550 °C [26], which is within the broad peak range observed in Fig. 2(a-1). In addition, the CuSe sample after high-temperature heating was subjected to the same DSC test again, with the results shown in Fig. 2(a-2). It is found that the sample has been completely changed, and the peaks observed in the first DSC test did not appear in the second test. A new peak appeared at 1127 °C that corresponds to the melting point of Cu<sub>2</sub>-Se. This shows that the CuSe decomposes more easily. Nevertheless, some CuSe was still present in the relatively lowtemperature range during the heating process. The DSC results for the Ag<sub>2</sub>Se powder are shown in Fig. 2(b). The endothermic peak at approximately 887 °C corresponds to the melting peak of Ag<sub>2</sub>Se. The melting point of Ag<sub>2</sub>Se is much higher than that of CuSe. Fig. 2 (c and d) shows the DSC results for CuInSe2 and AgInSe2, respectively. Two endothermic peaks are observed for both CuInSe2 and AgInSe<sub>2</sub>. The endothermic peak located at the lower temperature is the phase transition peak, and the peak at the higher temperature is the endothermic melting peak. It is observed that the melting point of AgInSe<sub>2</sub> of 633 °C is significantly lower than that of CuInSe<sub>2</sub> (932 °C), and is also lower than that of Ag<sub>2</sub>Se. It appears that the melting point for AgInSe<sub>2</sub> of 633 °C is slightly higher than the annealing temperature. Considering low gas pressure in the annealing process, the actual melting point for AgInSe2 should be lower than the annealing temperature. In addition, since the reaction of the metal precursors with Se is a typical exothermic compound reaction, the temperature of the films will rise during the reaction. This means that although the formation of CuSe with a low melting point is the origin of the promotion of grain growth

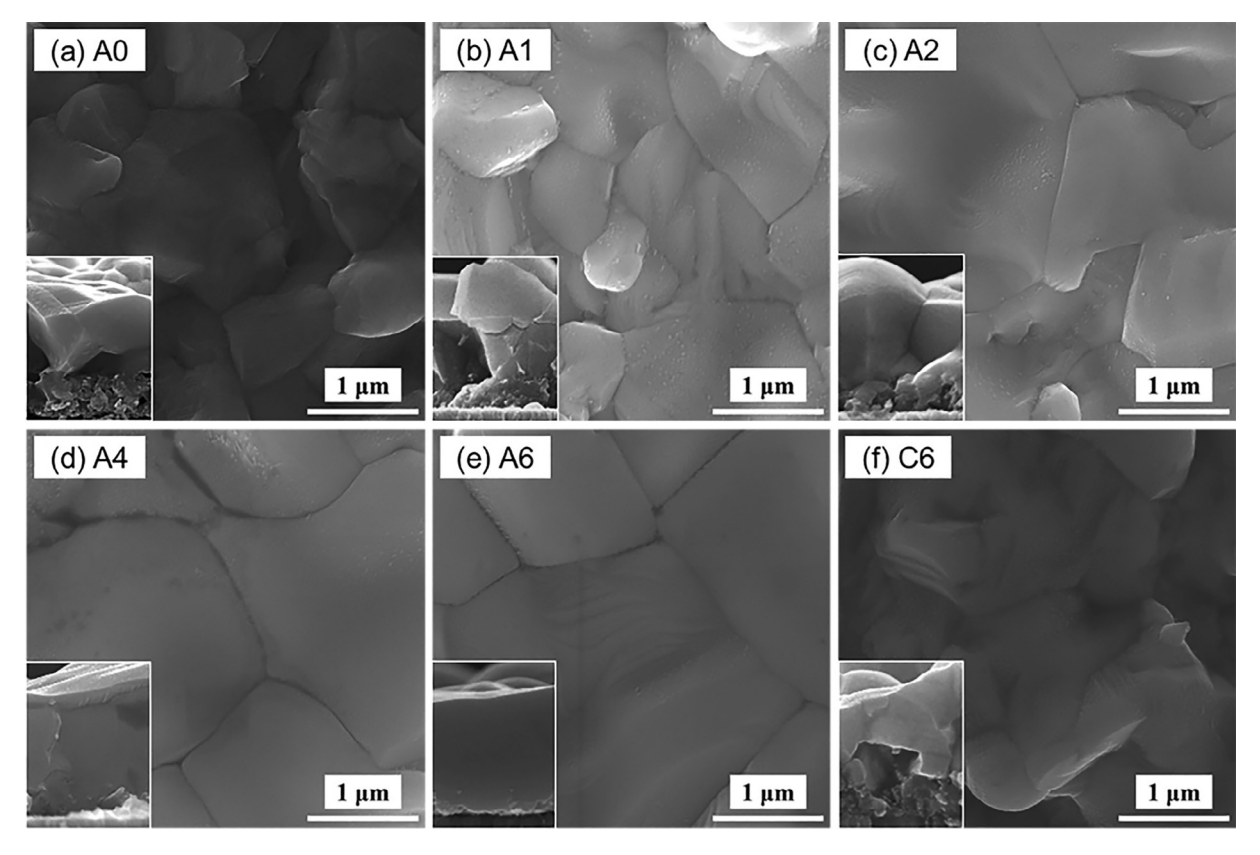


**Fig. 1.** The surface and cross-sectional SEM images of absorbers with different AAC of (a) A0, (b) A1, (c) A2, (d) A4, and (e) A6, respectively. (f) presents the surface and cross-sectional SEM images of the sample C6, in which the Ag in A6 is replaced with the equivalent amount of Cu.

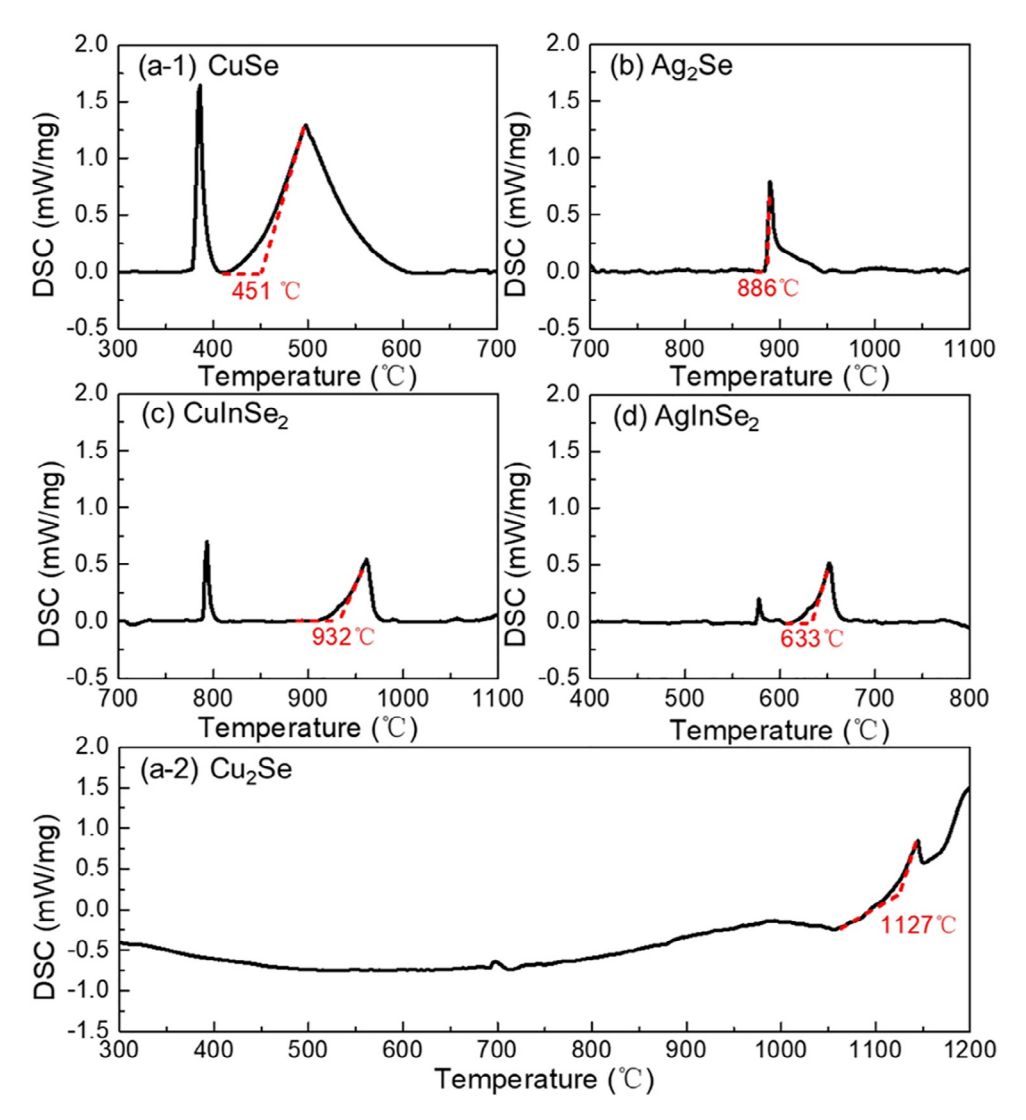


Fig. 2. DSC patterns of (a-1) CuSe, (b) Ag<sub>2</sub>Se, (c) CuInSe<sub>2</sub>, (d) AgInSe<sub>2</sub>, (a-2) Cu<sub>2</sub>Se.

by Cu, for the Ag addition the most important liquid phase to promote grain growth is not the Ag<sub>2</sub>Se phase but rather the AgInSe<sub>2</sub> phase.

The speed of the grain boundary migration (V) can be expressed by the following formula,

$$V = \frac{D}{\lambda} \left( -\frac{\Delta \mu}{kT} \right)$$

where D is the diffusion coefficient of the atom,  $\lambda$  is the distance of the atom migration,  $\Delta \mu$  is the free energy difference between the adjacent grains, k is the Boltzmann constant, and T is the temperature [27]. The values of  $-\Delta \mu/kT$  in the samples are similar when the addition of Cu or Ag is used as the control variable. In the samples with added Cu, some additional low-melting CuSe will appear. The Cu and Se atoms in liquid CuSe phase have high diffusion coefficients. Simultaneously, some other atoms can also migrate and diffuse through the liquid phase, and have a higher diffusion coefficient than that in the solid-phase state. In the samples with Ag doping, additional AgInSe2 or Ag(In,Ga)Se2 phases with a low melting point are present. Similarly, the Ag, In, Ga, and Se atoms in the liquid phase will also show stronger diffusion. Compared to the sample with Ag is composed of more elements. This means that

more atoms have a high diffusion coefficient. Fig. 3 shows the simulation diagram of atom migration. It is known that other atoms in the Cu-added sample must migrate from one crystal grain to another. In this process, they are scattered by Cu and Se atoms, and thus have a larger  $\lambda$ . For the atoms in the Ag-doped sample, since the atoms in the crystal grains are also present in the liquid phase, simple replacement can realize the migration of the atoms from one crystal grain to another. The  $\lambda$  values for the atoms in Ag-doped samples are much smaller. Therefore, according to the above formula for V, the Ag-doped samples have the higher grain boundary migration speed, and finally show larger grains. In other words, the sample with Ag doping can obtain a similar grain size to that of the sample without Ag doping but at a lower annealing temperature or for a shorter annealing time. This means that the Ag doping process is highly advantageous and beneficial due to reduced energy consumption, enabling the use of low meltingpoint substrates for the preparation of flexible solar cells, and obtaining improved production efficiency.

It is well-known that the grains of a CIGS film can grow further through the increase in the Cu concentration. However, excessive Cu will lead to the Cu-Se binary phase becoming a stable final product in the film rather than only an intermediate product of the annealing reaction [10]. This residual Cu-Se phase will act as a recombination center of excited charge carriers. Therefore, the Cu

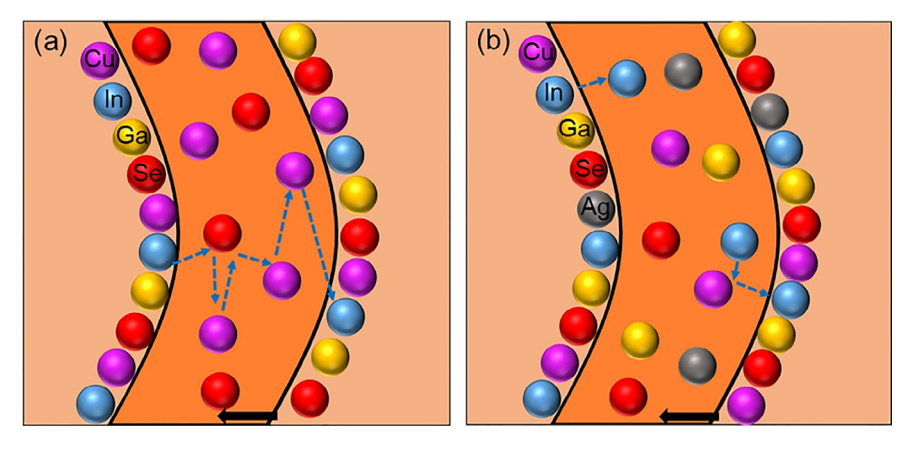


Fig. 3. Schematic diagram of atomic diffusion and grain boundary movement in (a) Cu-added samples and (b) Ag-doped samples. The blue dashed arrows represent the path of atoms diffusion. The solid black arrows represent the direction of the grain boundary movement.

concentration in CIGS cannot be too high. Although the mechanism of Ag doping for the promotion of grain growth is different from that of Cu addition, the residual phase may also occur in the Agdoped films. Therefore, films with the I/III group element ratio of 0.97 were obtained by sputtering a Cu target or an Ag target based on the CGI = 0.84 target. Fig. 4(a) shows the Raman spectra of the samples. Residual Cu-Se phases were observed in the Cu-added sample, while Ag-Se and Cu-Se phases were absent in the Agdoped sample treated with the same annealing process. The peak frequency of sample A20 is lower than that of sample C20 due to Ag doping [28]. Combined with the previous analysis, these results provide additional support for the mechanism of Ag promoting grain growth and indicate that Ag promotion of grain growth is mainly due to the effect of the AIGS phase.

According to the XRD patterns shown in Fig. 4(b), Ag doping did not cause a significant shift in the peak position. This is because only a small amount of Ag was doped into the samples. In addition, it is observed from Fig. 4(b) that all of the samples are composed of the pure chalcopyrite phase. Combined with the Raman results, these results suggest that the addition of Ag does not introduce impurity phases. The full width at half-maximum (FWHM) of the main peak shown in Fig. 4(c) changes with the increase of AAC. Fig. 1 shows that grains grow with increasing Ag amount. However, unlike the grain size, the FWHM did not change monotonically but rather first decreased and then increased. The addition of Ag can significantly improve the crystallinity of the film. Therefore, with the increase of Ag, the FWHM decreased within a specific range.

As the Ag amount continue to increase, although the grain size continues to increase, the FWHM increases. This is because the replacement of Cu with excessive Ag will introduce lattice distortion. The microscopic strain and microscopic stress generated by the lattice distortion eventually lead to the increase of the FWHM. The excessive microscopic strain will cause non-negligible structural defect that will affect the device performance similar to the grain boundaries. However, this phenomenon appears to have been rarely noticed in the study of Ag doping.

In addition to the aggravation of lattice distortion,  $Ag_{in}$  (or  $Ag_{Ga}$ ) substitution defects may be generated due to excessive Ag doping. Similar defects have been explored in the study of films with high Cu concentration [29,30]. However, the Ag-related substitution defects have not been reported to date. In this work, PL measurements were used to study the effects of Ag doping on the defect energy levels.

The obtained PL spectra are presented in Fig. 5(a) and show significant changes due to Ag doping. With increasing Ag concentration, the intrinsic PL peak position gradually shifts towards higher energy. PL is a surface characterization technique, and the shift of its intrinsic peak position is strongly related to the change of the near-surface band gap (Eg) of the film. In this work, both AAC and GGI will affect the value of Eg. The composition at the film surface was examined by EDS measurements. Based on the composition obtained, the Eg of  $(Ag_w,Cu_{1-w})(In_{1-x},Ga_x)Se_2$  can be calculated as  $Eg[eV] = 0.25w^2 + 0.03w + 0.08x^2 + 0.16x-0.11xw + 1.01$  [31]. Fig. 5(c) shows the relationship between the AAC, GGI and Eg. First,

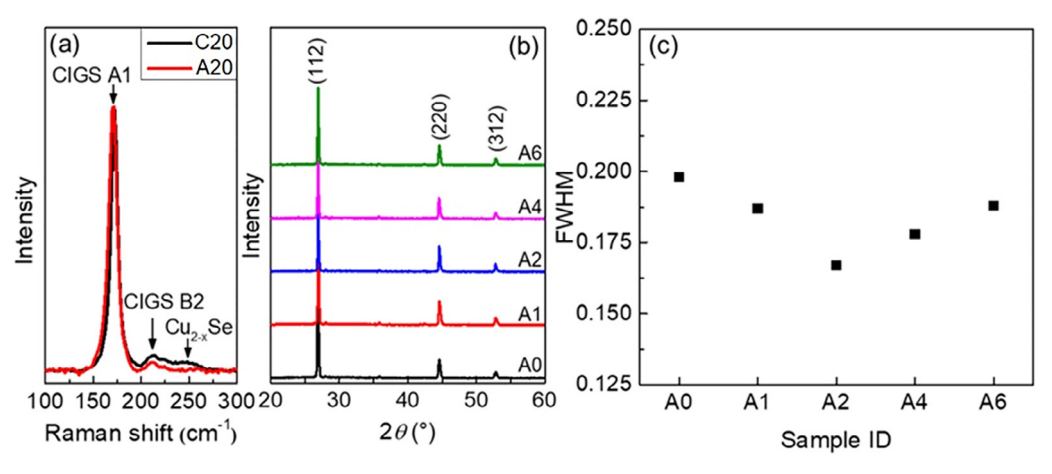


Fig. 4. (a) The Raman spectra of the sample A20 and sample C20. (b) The XRD patterns of the sample A0-A6, respectively. (c) FWHM values calculated from (b).

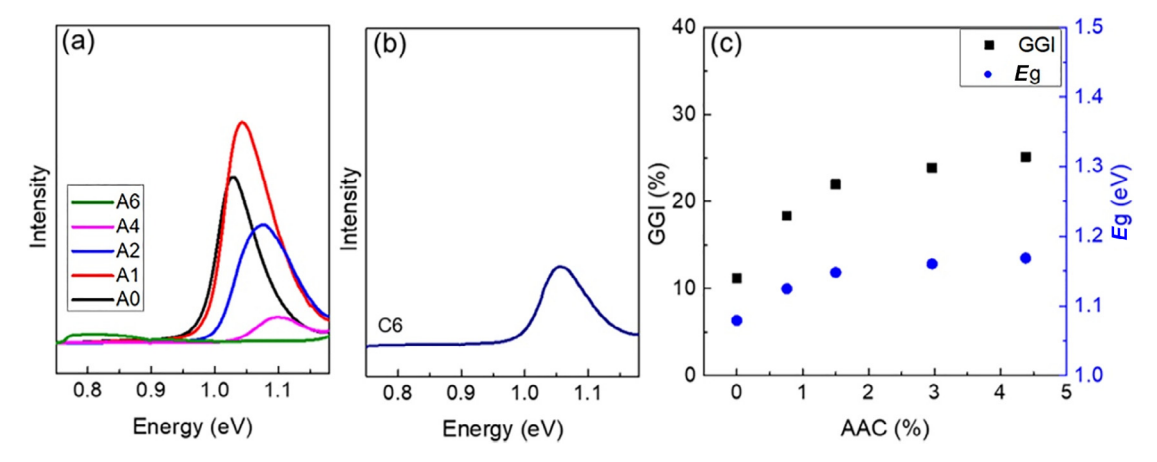


Fig. 5. (a) PL spectra of the absorbers with different AAC of A0–A6, respectively. (b) The PL spectrum of sample C6, in which the Ag in A6 is replaced with the equivalent amount of Cu. (c) The value of GGI and Eg with different AAC.

the calculated *Eg* value is close to the position of the intrinsic PL peak. The origin of the PL peak shift to higher energy was confirmed. On the other hand, it is clear that the more critical factor causing the change in near-surface *Eg* is the change in the GGI of the film surface. While the substitution of Ag itself can increase the *Eg* of the absorber, due to the small amount of Ag doping, it cannot cause significant changes in *Eg*.

The origin of the gradual increase of GGI on the surface with the doping of Ag is analyzed next. It is related to ability of Ag to promote the diffusion of Se atoms and Ga atoms as described above. Since the formation energy of CIS is smaller than that of CGS, Ga will be driven to the interface between the absorber and the Mo layer. Therefore, a gradient distribution of Ga appears with lower Ga content at the surface and greater Ga content at the back surface in the samples examined in this work. The promotion of the Se atom diffusion means that Se can enter the bottom layer from the surface of the absorption layer more quickly, and the compound reaction of Se can be completed more rapidly. Therefore, the driving force for Ga enrichment toward the back of the CIGS absorber disappears more quickly. After the reaction is completed, another driving force appears for Ga to return to the surface due to the concentration gradient of Ga. With the increase of AAC, the diffusion ability of Ga atoms gradually increases. Therefore, the distribution of Ga will be more uniform in the same time. Finally, the near-surface Ga-poor phenomenon is gradually alleviated, and GGI gradually increases. This confirms the origin of the PL peak position shift to the higher energies. Moreover, for a small amount of doped Ag, the intensity and integrated area of the PL peak increase. This indicates a reduction in non-radiative recombination.

For AAC >0.44, the PL spectrum changed dramatically. Not only the intensity of the intrinsic excitation peak is significantly reduced, but a new PL peak appears at the lower energy position. The difference between the intrinsic peak and the lower energy peak is approximately 0.3 eV. This deep-level defect was caused by the increase in the Ag concentration. To further determine the defect level, a sample with the same Cu addition was also examined by PL measurements. The PL peak of the defect level does not appear in the Cu-added sample. Based on the position of the energy level and experimental conditions, it is concluded that the defect is  $Ag_{In}$  (or  $Ag_{Ga}$ ) substitution defect [28]. Since the difference between the atomic radius of Ag and the atomic radius of In or Ga is smaller than that of Cu atoms, Ag<sub>In</sub> (or Ag<sub>Ga</sub>) defects are easier to form. Ag<sub>In</sub> (or Ag<sub>Ga</sub>) is a deep-level recombination center that will degrade carrier transport and thus its presence will degrade device performance.

In addition to the  $Ag_{in}$  (or  $Ag_{Ga}$ ) recombination center that negatively impacts the carriers transport, changes in the grain size and micro strain will also affect the transport and lifetime of the carriers. To characterize the quality of the film more comprehensively, Urbach energy ( $E_{U}$ ) and EIS measurements were performed with the results presented in Fig. 6.

 $E_{\rm U}$  is an interesting physical property of the absorber that can be estimated from the external quantum efficiency (EQE) at the long wavelength's edge [32] and can be used to characterize the transitions between Urbach tails. The transitions are affected by sub-gap absorption of the absorber. Therefore, many studies have shown that the  $E_{\rm U}$  can reflect the band tailing states of the device that can be used to evaluate the device quality [32,33]. With the addition of Ag, the  $E_U$  of the sample changed. When the Ag concentration is low, the value of  $E_U$  gradually decreases with the addition of Ag as shown in Fig. 6(a) and (b). This means that the quality of the film is improved, and the lifetime of the carriers is enhanced. This is mainly due to the contribution of Ag to grain growth and the passivation of non-radiative recombination. However, the  $E_U$  of the film increases drastically when Ag doping is excessive. This is primarily due to the non-negligible micro strain and Ag<sub>In</sub> (or Ag<sub>Ga</sub>) recombination centers caused by excessive Ag. All of these effects lead to band tailing and performance degradation. In addition, an examination of the open-circuit voltage deficit ( $V_{OC, def}$ ) presented in Fig. 7(c) shows that the  $V_{\rm OC, def}$  is close related to  $E_{\rm U}$ . For samples with larger  $E_U$ , the saturation current density  $(J_0)$  is larger, resulting in larger  $V_{\rm OC, def}$ . Finally, the  $E_{\rm U}$  of sample A2 reached 11.7 meV, which is the minimum value obtained in this work. At the same time, sample A2 exhibited the smallest  $V_{\rm OC, def}$ .

Generally, the classic Nyquist chart is composed of one or more semicircular arcs with a specific diameter along the Z' axis. The semicircle has two intercepts with Z' axis, and the smaller intercept can characterize the series resistance (Rs) of the device. According to Fig. 6(d), Ag doping will cause a slight increase in Rs. The diameters represent the carrier recombination resistance (Rc) [34,35]. As the Ag concentration increases, the largest change is observed in the diameters of the semicircles. This indicates that Ag doping has a significant effect on carrier recombination. As shown in Fig. 6(d), the diameter first increases and then decreases with increasing Ag concentration. This also implies that the Rc and carrier lifetime first increase and then decline. According to the work of Bisquert [36], the minority carrier lifetime is equal to the product of the Rc and the composite capacitance (C). The values of Rc and C can be obtained by fitting the EIS curve. Based on the calculation, the minority carrier lifetimes of the samples can be obtained as 0.262, 49.5, 51.4, 28.3, 0.213 µs, respectively. This

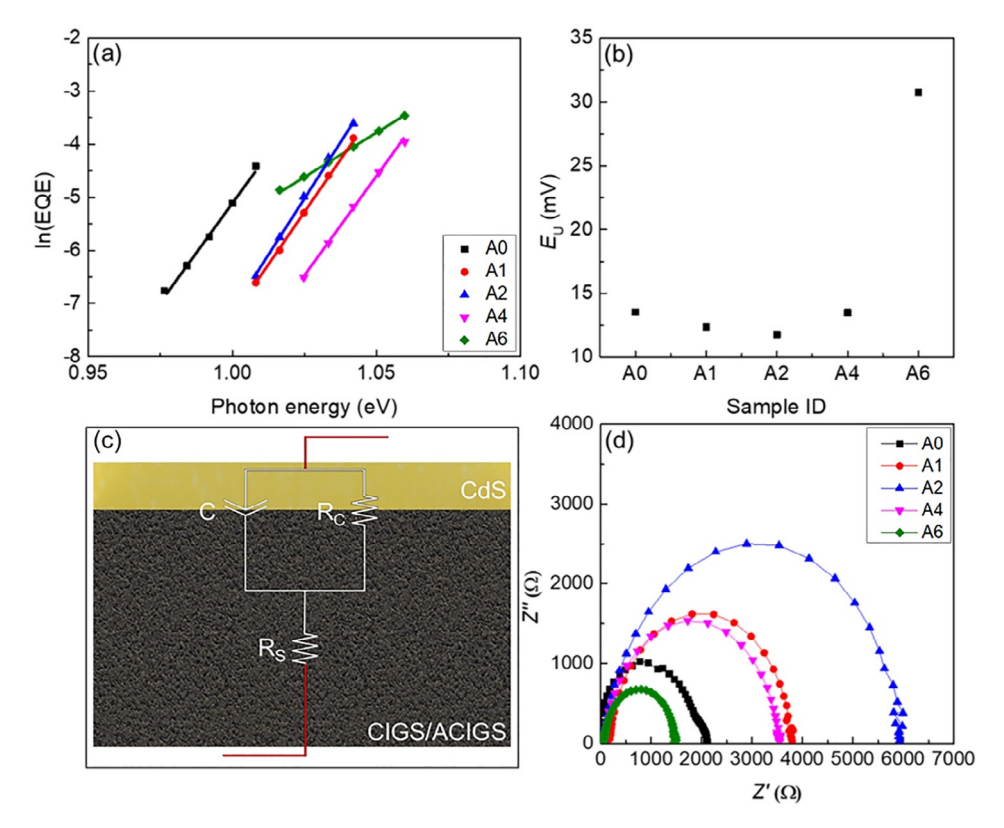


**Fig. 6.** (a) ln(EQE) in the long-wavelength edge (near the band edge) and (b)  $E_U$  values of solar cells with different AAC of A0–A6, respectively. (c) Model circuit appropriate with the experimental impedance data for the samples. (d) Electrochemical impedance spectra of devices A0–A6.

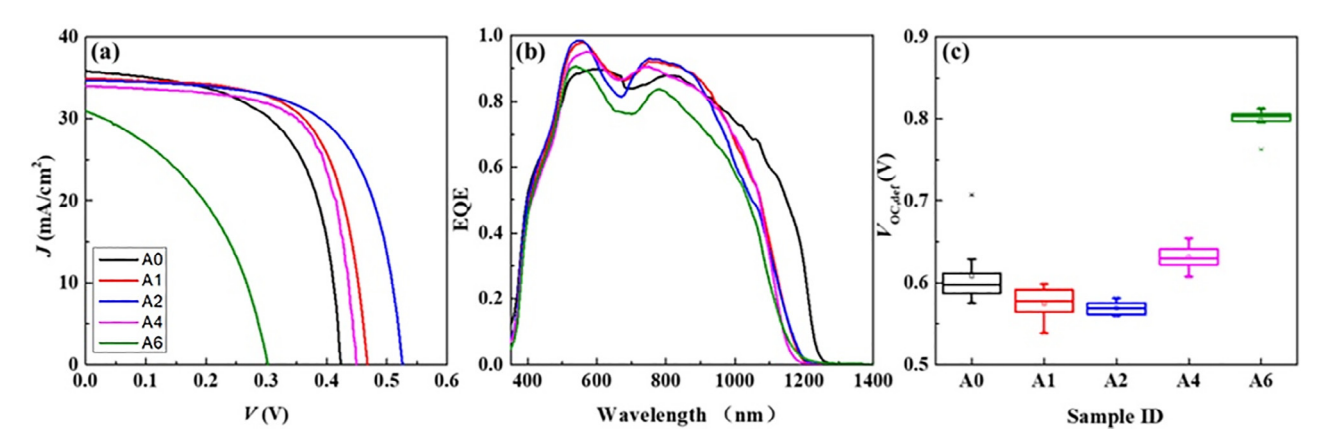


**Fig. 7.** (a) Typical J-V characteristics of the representative solar cells with different AAC of A0–A6. (b) EQE spectra of the solar cells with different AAC of A0–A6. (c)  $V_{\rm OC, \ def}$  of the cells with various AAC of A0–A6.  $V_{\rm OC, \ def}$  is the value of Eg/q- $V_{\rm OC}$ , and the Eg is obtained by PL measurement. Every boxplot was based on more than five cells.

means that appropriate Ag doping can increase the diffusion length of minority carriers which is beneficial for their collection. However, the beneficial effect of Ag doping decreases when AAC >0.030. For AAC >0.044, Ag doping will degrade the transport and collection of carriers. This is consistent with the results of  $E_{\rm U}$  measurements and other characterizations.

The quality of the absorber strongly affects device performance. Fig. 7(a) shows the J-V curves of the devices fabricated using samples with different Ag concentrations. Inevitably, there are differences between the samples. Overall,  $J_{SC}$  is reduced upon Ag doping because Ag doping enhances atom diffusion and inhibits the enrichment of Ga at the interface between the absorber and the back electrode. Additionally, the presence of Ag also increases Eg. Thus, the Eg of the superficial layer is increased. Correspond-

ingly, the cutoff wavelength of the EQE shifts toward shorter wavelengths in Fig. 7(b). The EQE difference in the long-wavelength range is also due to this effect. The increase in the grain size and the improvement of film quality caused by Ag doping increase the EQE values of samples A1, A2 and A4 in the 500–1000 nm wavelength range. The quality of the absorber and device of sample A6 is poor, so that its EQE value is lower. Although the increase in crystallinity is beneficial for increasing EQE within a certain range and reduces the scattering of carrier transport, the increase in Eg appears to give rise to a greater reduction in  $J_{SC}$ . Moreover, the increasing series resistance with Ag doping also reduces  $J_{SC}$ . The increase in Eg also increases the  $V_{OC}$ . In addition to being affected by Eg,  $V_{OC}$  is also affected by the aforementioned structural defects, namely the Ag<sub>In</sub> (or Ag<sub>Ga</sub>) substitution defects, and the band tailing

states. Therefore,  $V_{\rm OC}$  changes did not show a single trend change and achieved the highest  $V_{\rm OC}$  value was achieved for AAC of 0.015 (sample A2). The device with the best device performance in the work was also obtained at AAC of 0.015.

#### 4. Conclusions

In this work, the CIGS samples with different concentration of Ag doping were fabricated. The effects of Ag on film quality and device performances were explored. It was found that Ag doping can lower the melting point of the absorbers. This promotes the diffusion of elements and grain boundary migration, and leads to improved crystallinity. The phenomenon of Ga enrichment at the interface between the absorber and the back electrode is also suppressed. The non-radiative recombination of the film gradually decreases with the increase in the Ag amount for AAC < 0.015. The band tail absorption is also suppressed, and the film quality is gradually improved, leading to reduced recombination and improved carrier transport. However, a too high amount of doped Ag will have negative effects on the film properties. For AAC  $\geq$  0.030, micro strain appears and increases in the film due to Ag doping. The  $E_U$  value will also gradually increase. For  $AAC \ge 0.044$ ,  $Ag_{In}$  ( $Ag_{Ga}$ ) defects appear in the films. Therefore, the excessive addition of Ag will increase the carrier recombination rate and  $V_{\rm OC, def}$ . In this compositional range, the performance of the device is even lower than that of the un-doped sample. For the CIGS fabricated by the annealing of the CuInGa precursor films in this work, the optimal value of AAC is approximately 0.015.

## **Declaration of Competing Interest**

The authors declare that they have no known competing financial interests or personal relationships that could have appeared to influence the work reported in this paper.

# Acknowledgment

This work was supported by the analysis support of the State Key Laboratory of New Ceramics and Fine Processing.

#### References

- [1] M. Nakamura, K. Yamaguchi, Y. Kimoto, et al., J. Photovolt. 9 (2019) 1863-
- [2] R. Carron, S. Nishiwaki, T. Feurer, et al., Adv. Energy Mater. 9 (2019) 1900408.
- [3] W. Zi, Z. Jin, S. Liu, et al., J. Energy Chem. 27 (2018) 971-989.
- [4] T.-M. Hsieh, S.I. Lue, J. Ao, et al., J. Power Sources. 246 (2014) 443–448.
- [5] J. Qu, L. Zhang, H. Wang, et al., Opt. Quant. Electron. 51 (2019) 383.
- [6] H. Lee, Y. Jang, S.-W. Nam, et al., ACS Appl. Mater. Inter. 11 (2019) 35653-35660
- [7] C.-H. Hsu, W.-H. Ho, S.-Y. Wei, et al., Adv. Energy Mater. 7 (2017) 1602571.
- [8] I.J. Choi, J.W. Jang, B.C. Mohanty, et al., ACS Appl. Mater. Inter. 8 (2016) 17011-17015.
- [9] T. Nishimura, S. Toki, H. Sugiura, et al., Prog. Photovolt, 26 (2017) 291-302.
- [10] E.S. Sanli, Q.M. Ramasse, R. Mainz, et al., Appl. Phys. Lett. 111 (2017) 032103.
  [11] X. Peng, M. Zhao, D. Zhuang, et al., Vacuum. 152 (2018) 184–187.
- [12] T. Lepetit, S. Harel, L. Arzel, et al., Prog. Photovolt. 25 (2017) 1068–1076.
- [13] H. Elanzeery, M. Melchiorre, M. Sood, et al., Phys. Rev. Mater. 3 (2019) 055403.
- [14] J. Ramanujam, U.P. Singh, Energy Environ, Sci. 10 (2017) 1306–1319.
- [15] S.-W. Chen, J.-S. Chang, Ssu-ming Tseng, et al. J. Alloy. Compd. 656. 2016. 58-66.
- [16] N. Valdes, J. Lee, W. Shafarman, Sol. Energ. Mat. Sol. 195 (2019) 155-159.
- [17] X. Zhang, M. Kobayashi, A. Yamada, ACS Appl. Mater. Inter. 9 (2017) 16215-16220
- [18] X. Zhao, X. Chang, D. Kou, et al., J. Energy Chem. 50 (2020) 9–15.
   [19] Y. Zhao, S. Yuan, D. Kou, et al., ACS Appl. Mater. Inter. 12 (2020) 12717–12726.
- [20] J. Zhai, H. Cao, M. Zhao, et al., Ceram. Int. 47 (2021) 2288-2293.
- [21] C. Wang, D. Zhuang, M. Zhao, et al., J. Power Sources. 479 (2020) 229105.
- [22] C. Wang, D. Zhuang, M. Zhao, et al., Sol. Energy. 194 (2019) 11-17.
- [23] Y. Yuan, L. Zhang, G. Yan, et al., ACS Appl. Mater. Inter. 11 (2019) 20157-20166
- [24] X. Zhang, D. Han, S. Chen, et al., J. Energy Chem. 27 (2018) 1140-1150.
- [25] U. Chalapathi, M.A. Scarpulla, S.-H. Park, et al., J. Mater. Sci. Mater. Electron. 30 (2019) 4931-4935.
- [26] H. Komaki, M. Iioka, A. Yamada, Jpn. J. Appl. Phys. 51 (2012) 10NC04.
- [27] Y. Li, J. Xiong, B. Tao, et al., in: Materials Physics, Science Press Ltd., Beijing, 2016, pp. 169-170.
- L. Zhang, T. Li, H. Wang, et al., Superlattice. Microst. 114 (2018) 370-378.
- [29] J.-F. Guillemoles, U. Rau, L. Kronik, et al., Adv. Mater. 11 (1999) 957-961.
- [30] M. Marudachalam, R. Birkmire, H. Hichri, et al., J. Appl. Phys. 82 (1997) 2896-2905
- [31] K. Kim, J. Park, J. Yoo, et al., Sol. Energ. Mat. Sol. 146 (2016) 114-120.
- [32] J. Chantana, Y. Kawano, T. Nishimura, et al., Sol. Energ. Mat. Sol. 210 (2020) 110502.
- [33] J. Jean, T.S. Mahony, D. Bozyigi, et al., ACS Energy Lett. 2 (2017) 2616-2624.
- [34] C.R. Dhas, A.J. Christy, R. Venkatesh, et al. Thin Solid Films. 653. 2018. 73-81.
- [35] G. Wang, W. Zhao, Y. Cui, et al., ACS Appl. Mater. Inter. 5 (2013) 10042-10047.
- [36] J. Bisquert, F.F. Santiago, I.M. Seró, et al., J. Phys. Chem. C. 113 (2009) 17278-17290